Intercalation into mesoporous materials that contain transition metals (e.g., niobium oxide) allows the production of a variety of structures with unique properties.

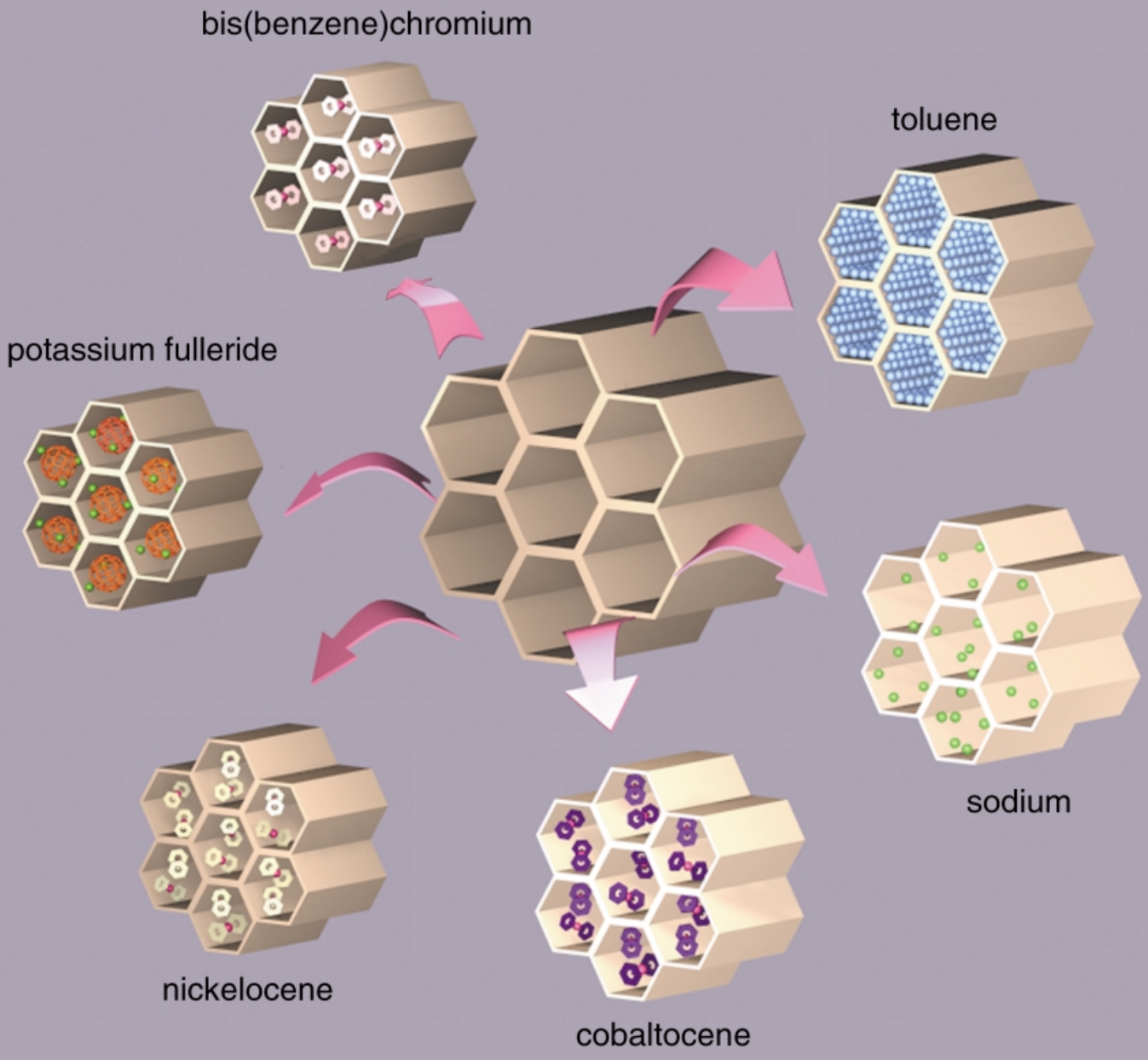

ANGEWANDTE CHEMIE

Recent Advances in Synthesis and Applications of Transition Metal Containing Mesoporous Molecular Sieves

Xun He and David Antonelli*

Work in mesoporous silica-based materials began in the early 1990s with work by Mobil. These materials had pore sizes from 20 – 500 Å and surface areas of up to 1500 $m^2 g^{-1}$ and were synthesized by a novel liquid crystal templating approach. Researchers subsequently extended this strategy to the synthesis of mesoporous transition metal oxides, a class of materials useful in catalysis, electronic, and magnetic applications because of variable oxidation states, and populated d-bands—features not found in silicates. These materials are already showing promise in electronic and optical applications hinging on the semiconducting properties of transition metal oxides and their potential to act as electron acceptors, an important feature in the design of cathodic materials. This is the first general review of non-silicate mesoporous materials and will focus on recent advances in this area, emphasizing materials possessing unique electronic, magnetic, or optical properties. Also covered are advances in the synthesis and applications of mesostructured sulfides as well as a new class of template-synthesized platinum-based materials that show promise in heterogeneous catalysis.

Keywords: electronic properties · mesoporous materials · semiconductors · solid-state structures · template synthesis

1. Introduction

In the wake of a great expansion of interest in the design and synthesis of materials with tailored chemical and physical properties, materials scientists have focused much attention on shape-controlled composite materials, with the goal being to create systems in which there is functional cooperation between the overall nanoscale architecture of the material and its physical properties. Multilayered nanotubes,[1] imprinted polymers,[2] polymer-encapsulated drug delivery systems,[3] and "artificial leaf" technologies[4] are examples of systems that weave two or more disparate materials into a single whole, which possesses electronic, mechanical, or optical properties not possible in more simple single-phase bulk systems. A crucial feature in the design of many functional materials is controlled porosity over a broad length scale. Advances by Mobil researchers in the 1990s led to the discovery of MS41 mesoporous silicates, a family of materials with regularly spaced nanometer-sized pores, synthesized by using liquid crystals as structural imprints to cast the shape of the silica.[5–12] Since this work, researchers have expanded this basic motif to the point where it is possible to synthesize fabricated architectures with a myriad of structural features and pore sizes ranging from 1 – 10000 nm out of virtually any stable solid substance that can be easily manipulated on the nanoscale.[13] Single molecules,[14] self-assembled surfactant phases,[15] amphiphilic block copolymers,[16, 17] vesicles,[18] emulsion-stabilized oil droplets,[19] and even micron-level latex spheres[20, 21] have all been used in this regard, the last example being of particular importance to the fabrication of photonic band-gap materials.[22] Transition metals and transition metal oxides are of particular interest in the synthesis of ordered materials because of their variable oxidation states, properties not possessed by silicates, a capacity which often leads to unusual magnetic, electronic, and optical properties.

After pioneering efforts leading to the synthesis of mesostructured W and Pb oxides in 1993,[23] a stable mesoporous Nb oxide molecular sieve was reported in 1996.[24, 25] This material had an advantage over the W and Pb materials in that the pore structure remained intact after template removal. Shortly thereafter the synthesis of related mesoporous Zr, Ti, Ta, Hf, and Mn oxides,[26–38] were reported, the last example being of special note since it was the first such material with semiconducting properties,[38] an important feature in many catalytic and electronic applications. More recently, Ozin and co-workers reported the synthesis of mesoporous yttrium-doped zirconium oxide materials with high ion conductivity for fuel-cell applications.[39] Kanatzidis and co-workers[40] and

[*] Prof. D. Antonelli, X. He
Department of Chemistry and Biochemistry
University of Windsor
401 Sunset Avenue, Windsor, Ontario N9B-3P4 (Canada)
Fax: (+1) 519-973-7098
E-mail: danton@server.uwindsor.ca

  1433-7851/02/4102-0215 $ 17.50+.50/0

Ozin and co-workers[41] independently synthesized mesoporous Ge sulfide based materials with semiconducting properties. Research in our group has focused on the reduction and modification of existing mesoporous Nb, Ti, and Ta oxides,[42, 43] to lead to numerous organometallic/inorganic composites with semiconducting, metallic, superparamagnetic, and even spin-glass behavior. This review will focus principally on these and other recent advances in electroactive molecular sieves, an exciting and rapidly growing area of research interest.

2. Electroactive Mesoporous Transition Metal Oxides

2.1. Mesoporous Zirconium Oxide Based Systems for Fuel-Cell Applications

Solid oxide fuel cells (SOFC) have attracted much recent attention in the fields of materials science, catalysis, ceramics, and electrochemistry.[44] Much of this research is aimed at the design of electrode materials which are not only stable under high operating temperatures (600–1000 °C), but also have optimal electronic and ionic conductivity coupled with catalytic activity and mass-transfer properties. The traditional electrode materials are nickel/yttrium oxide-stabilized-zirconium oxide (Ni-YSZ) cermet (ceramic/metal) as the anode and perovskite or platinum/yttrium oxide-stabilized-zirconium oxide (Pt-YSZ) as the cathode. The common approach to improve the performance of the materials is to enlarge the triple-phase boundary (TPB), which controls the efficiency of the SOFCs, by decreasing the dimensions of the active metal particles, Ni or Pt, relative to that of the yttrium oxide-stabilized-zirconium oxide grains. Several researchers have attempted to improve the porosity and enlarge the TPB of the materials by manipulating the microstructure of electrode materials through traditional nanofabrication techniques,[45] but most of these materials are just nanoscale or microscale versions of the bulk cermet electrode ceramics with a comparatively low thermal stability and wide pore-size distribution.

Ozin's group recently reported the first example of binary and ternary mesoporous yttrium oxide-stabilized-zirconium oxide (meso-YSZ) and metal (Pt, Ni)- yttrium oxide-zirconium oxide solid solutions which could be used as solid oxide fuel-cell electrode materials.[39, 46, 47] While much work has gone into the synthesis of stable mesoporous zirconium oxides, including an elegant recent example from Rao's group[48] demonstrating an unusual lamellar-to-hexagonal-to-cubic phase change (Figure 1), these materials differ from previous efforts in that they use yttrium as a stabilizing agent. These mesoporous yttrium oxide-stabilized-zirconium oxide materials were synthesized by modified sol–gel methods under basic conditions, where zirconium ethoxide and yttrium acetate were used as the precursors for the transition metal oxides, and the cationic surfactant, cetyltrimethylammonium bromide (CTAB) was used as the mesostructure-directing reagent. The higher dielectric constant and coordinating ability of ethylene glycol was able to control the rate of hydrolysis and avoid the solubility problems which previously resulted in low levels of yttrium oxide incorporation in the zirconium oxide phase.[49] The surfactant template was removed by calcining the as-synthesized materials at various

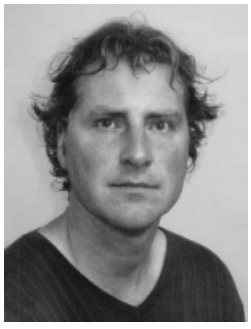

D. Antonelli

X. He

David Antonelli was born in Chicago in 1963 and raised in The United States, Great Britain, and Canada. He completed his BSc at the University of Alberta in 1987 and his PhD in organometallic chemistry with Martin Cowie at the University of Alberta three years later at the end of 1990. He was an NSERC postdoctoral fellow in organometallic chemistry at Oxford University with M. L. H. Green in 1991, and at Caltech in 1992–93 with John E. Bercaw. After completing a postdoctoral term in Ziegler-Natta catalysis with Jeffrey Stryker at the University of Alberta in 1993, he moved on to study nanoporous materials as a postdoctoral associate with Prof. J. Y. Ying at the Massachusetts Institute of Technology Department of Chemical Engineering from 1994–1996. In 1997 he took up a lectureship at The University of Sussex School of Chemistry, Physics, and Environmental Science before returning to Canada in 1998 as an Associate Professor in Chemistry at the University of Windsor. He currently directs a research group focused on the electronic and catalytic properties of nanoporous materials with variable oxidation states and conducting molecular wires in the pores. He is the author of over 40 publications and was the winner of the Ontario Premier's Research Excellence Award, The University of Windsor Excellence in Research and Scholarship Award, and a Royal Society of Britain Research Award.

Xun He obtained a B.S. degree in organic chemistry at Southwest China Normal University (1989–1993), a M.S. degree in surfactant Chemistry at Institute of Chemistry, the Chinese Academy of Sciences (1993–1996), and then worked in the Chinese Academy of Sciences for three years. He joined Dr. Antonelli's group as a graduate in 1999. His present research project focuses on the synthesis and characterization of electro-active mesoporous materials.

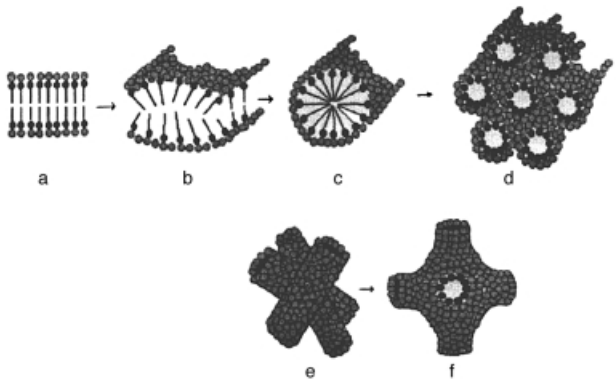

Figure 1. Schematic representation of lamellar-to-hexagonal phase transformation (a – d) and the hexagonal-to-cubic transformation (e and f) in mesostructured zirconium oxide. Reproduced with permission from ref. [48].

rates and temperatures. The yttrium content in these binary materials can be tuned from 12 – 56 wt % and no phase segregation of yttrium oxide and zirconium oxide was observed. The nitrogen adsorption isotherms of these materials after calcination gave Brunauer – Emmett – Teller (BET) surface areas ranging from 100 – 300 $m^2 g^{-1}$, and an average pore size of 18 – 21 Å. The pore wall was determined to be 25 – 28 Å thick and composed of nanocrystalline yttrium oxide-stabilized zirconium oxide. The synthetic strategy is outlined in Figure 2. The variable-temperature powder X-ray diffraction patterns illustrated the high structural stability of these materials at temperatures above 600 °C, a property crucial for useful solid oxide fuel-cell materials. This material possesses the highest surface area of any recorded sample of template-free yttrium oxide stabilized zirconium oxide.

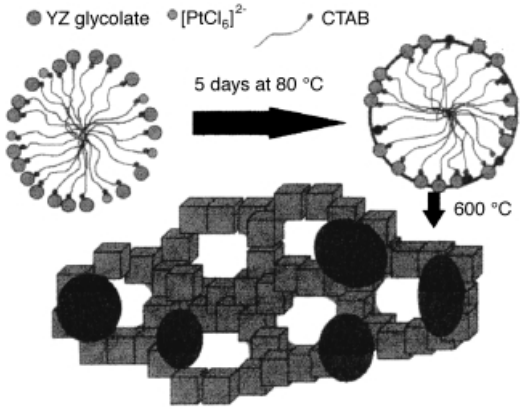

Figure 2. Self-Assembly of anionic yttrium – zirconium glycolate and hexachloroplatinate precursors with a supramolecular cationic surfactant template leading to the formation of a mesoporous material denoted *meso*-PtYZ. Reproduced with permission from ref. [46].

Electroactive ternary mesoporous metal (Pt, Ni) yttrium oxide zirconium oxide, were synthesized by using metal precursors, such as sodium hexachloroplatinate, or Ni^{II} reagents, that is, bis(acetatato) nickel, nickel chloride, or nickel nitrate as the source of the third metal dopant in the presence of surfactant-containing yttrium oxide zirconium oxide gels.[46, 47] This method produced ternary transition metal oxides with pore structures similar to those of the meso-YSZ materials. The inclusion of Ni or Pt in the materials is necessary for applications in fuel cells, as it effects the charge-transfer and oxygen-transport properties. In these materials platinum and nickel exist as metal (Pt) and metal oxide (NiO_{1+x}) nanoclusters, respectively, 30 – 40 Å in size, homogeneously dispersed throughout the yttrium oxide zirconium oxide mesostructures. The amount of Pt and Ni can be tuned from 1-10 wt % and 10 – 30 wt %, respectively. A chemisorption titration experiment on meso-Pt-YSZ by use of $H_2 - O_2$ adsorbents showed that the surface area of the incorporated platinum nanoclusters was partly accessible to gaseous reagents and gave a representative dispersion of 18 % for a sample loading of 2.4 wt % Pt. The ionic conductivity of meso-Pt (NiO)-YSZ materials was evaluated by alternating current (AC) complex impedance spectroscopy in the temperature range of 300 – 800 °C and recorded in an air atmosphere. The meso-YSZ and meso-Pt-YSZ samples gave a single symmetric, slightly depressed semicircle from 500 – 700 °C, which results from both bulk and grain boundary polarization and all the meso-NiO-YSZ samples yielded similar impedance spectra. The bulk and grain boundary conductivity of all meso-Pt(NiO)-YSZ samples was extracted from the low-frequency minima of the respective semicircles in the Argand plots of the complex impedance spectra (Figure 3). The corresponding activation energies E_a for thermally activated charge-transported process were obtained from the Arrhenius equation $\sigma = (A/T)\exp(E_a/RT)$. These data are summarized in Table 1.

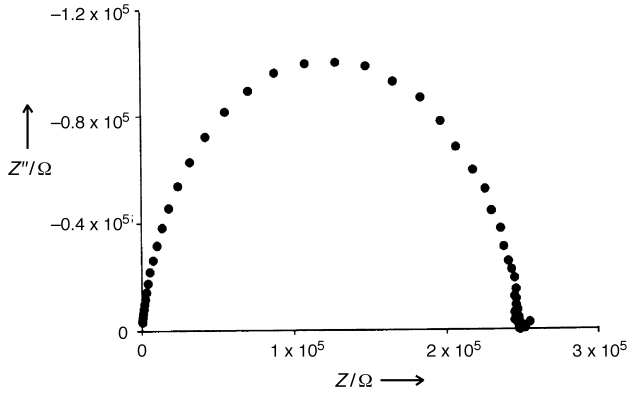

Figure 3. Complex impedance Argand plot for meso-NiO-YSZ with 22 wt % NiO recorded at 296 °C in air.[47]

Table 1. Conductivities (σ) [$\Omega^{-1}cm^{-1}$] and corresponding activation energies [$kJ\,mol^{-1}$] of mesoporous Pt(NiO)-YSZ samples.

	Pt-YSZ	Pt-YSZ	Pt-YSZ	Ni-YSZ	Ni-YSZ	Ni-YSZ
wt % (Pt or NiO)	2	17	23	7	22	27
E_a	207	130	93	67	53	36
σ(450 °C)	–	3.4×10^{-8}	5.5×10^{-5}	1.2×10^{-7}	6.2×10^{-6}	2.9×10^{-5}

The mixed oxygen-ion electron charge transport was dominated by the nonstoichiometric nickel oxide nanocrystalline phase at low temperature (around 400 °C) in the meso-NiO-YSZ. The enhanced NiO connectivity within meso-NiO-YSZ forms an electronic conduction pathway at far lower NiO content than in conventional materials (little change $E_a = 80 -$

100 kJ mol^{-1} with NiO content from 0–40 mol %). However, the slightly higher activation energies for oxygen ion charge transport in the meso-Pt-YSZ materials as compared to conventional Pt-YSZ were also observed maybe as a result of the nanocrystalline YSZ channel walls. These two materials represent a new class of solid fuel-cell electrode materials and show some of the first potential applications of mesoporous transition metal oxides.

2.2. Semiconducting Mesoporous Manganese Oxides

Transition metal oxides have variable oxidation states and d electrons, these properties offers advantages over aluminosilicate materials, thus the direct chemical syntheses of mesoporous transition metal oxides with partially filled d shells should lead to materials with unusual electronic, magnetic, and catalytic properties. However, most of the mesoporous transition metal oxides synthesized to date, including Ti,[32] Nb,[24, 25] Ta,[28] W,[23] Zn,[50] V,[51] Zr,[29–31] and Hf[33] are insulators containing high-valent transition metals in a single oxidation state. Recently Suib's group reported hexagonal and cubic phases of mesoporous manganese oxides with mixed oxidation states. These phases were synthesized using surfactants as mesostructure directing agents. These materials represented the first semiconducting mesostructures and possess catalytic activity in the oxidation of alkanes.[38] The mixed oxidation states (III/IV) of manganese in these materials result from the oxidation of the metal precursor $Mn(OH)_2$ (or $Mn(OH)_6^{4-}$) by air during the synthetic process. The calcined samples prepared with higher surfactant concentration (28 wt %) had hexagonally ordered manganese oxide channels (MOMS-1), while lower concentration (10 wt %) of surfactant resulted in cubic mesostructures (MOMS-2). The argon adsorption isotherms of MOMS-1 and MOMS-2 gave BET surface areas of 170 $m^2 g^{-1}$ and 46 $m^2 g^{-1}$, respectively, while the pore sizes and wall thicknesses were 30 and 17 Å, respectively. The walls of the mesopores are composed of microcrystallites of dense phase of Mn_2O_3 and Mn_3O_4 (average oxidation states of Mn in MOMS-1 is 3.55) with MnO_6 octahedra as the primary building blocks which are linked together by sharing edges. This is an important advance because most mesoporous materials possess amorphous walls, an undesirable feature in many catalyst supports. No other phases or amorphous manganese oxides were observed by transmission electron microscopy (TEM) or X-ray diffraction (XRD) methods. The conductivities of MOMS-1 before and after calcination are 5.0×10^{-8} and $8.1 \times 10^{-6}\ \Omega^{-1} cm^{-1}$, respectively (the band gap from UV spectra for the calcined material is 2.46 eV), while the conductivity of MOMS-2 is $2.28 \times 10^{-6}\ \Omega^{-1} cm^{-1}$. These materials were the first semiconducting mesostructures and for this reason may have applications in photocatalysis or the fabrication of novel optic and electronic devices. Thermogravimetric analysis (TGA) and differential scanning calorimetry (DSC) demonstrated that both MOMS materials are stable at up to 1000 °C. The Fourier transform infrared (FT-IR) data for pyridine adsorbed on calcined MOMS-1 indicate that there are two types of Lewis acid sites. This result is further supported by the observation that MOMS-1 can act as an active oxidation catalyst in the oxidation of cyclohexane and *n*-hexane to the corresponding alcohols in aqueous solutions.

2.3. Hierarchically Templated Mixed-Valent Molybdenum Oxides

In 1999 our group reported a semiconducting mesostructured mixed oxidation state molybdenum oxide, a material which selectively forms toroidal shapes with diameter of several hundred nanometers.[52] This material was prepared by use of an as-synthesized dimeric molybdenum ethoxide complex with a bridging dodecylimido group as structure-constructing blocks and then hydrolyzing to generate a bronze mesostructure Mo oxide. The XRD pattern showed a high intensity peak (100) at $d = 32$ Å. The X-ray photoelectron spectrum (XPS) displayed Mo $3d_{5/2}$ emissions which could be simulated as three peaks at 231.9, 232.8, and 230.9 eV. The peak at 232.8 eV can be assigned to Mo^V, and the gap from valance band to Fermi level is 1.3 eV (band gap calculated from UV is 3.75 eV), which provides evidence for weakly semiconducting properties in this material.

The toroidal structures of this material, which are constructed of oriented mesotubules of roughly 50 nm in length and 3 nm in diameter, were revealed by transmission electron microscopy (TEM) images (Figure 4a). The toroidal shapes were thought to arise from a double templating interaction where the amine template forms both micelles and vesicles or microbubbles under the same conditions.[53, 54] Attempts to remove the template either by acid treatment or ozone treatment led to the formation of layered and amorphous materials, respectively. Figure 4b shows TEM images which provide evidence for an unusual dynamic process in which adjacent toroids open up and coalesce into much larger toroids. This was the first example of dynamic behavior in such hierarchically ordered materials and is a similar process to that observed in bundles of carbon nanotubes at high temperature.[55]

When these bronze toroidal mesoporous materials were hydrothermally treated in a sealed tube at 150 °C for ten days, a phase changed to a new blue material consisting of 2–3 nm Mo^{IV} oxide crystallites (Figure 4c), thought to arise from crystallization of the walls, and a mesolamellar Mo^{VI} region (Figure 4d) as indicated by XRD and TEM. The conductivity of this blue material is $6.3 \times 10^{-7}\ \Omega^{-1} cm^{-1}$, higher than that of the bronze compound, possibly because of the presence of metallic Mo^{IV} oxide. The XPS supports the presence of a metallic phase with a weak emission near the Fermi level. While MOMS mesoporous manganese oxide materials possess crystalline walls, in the case of these molybdenum oxide toroids, crystallization of the walls leads to collapse of both the mesostructure and the macrostructure, which suggests that long-range order in the walls in many cases may come at the expense of the porous structure.

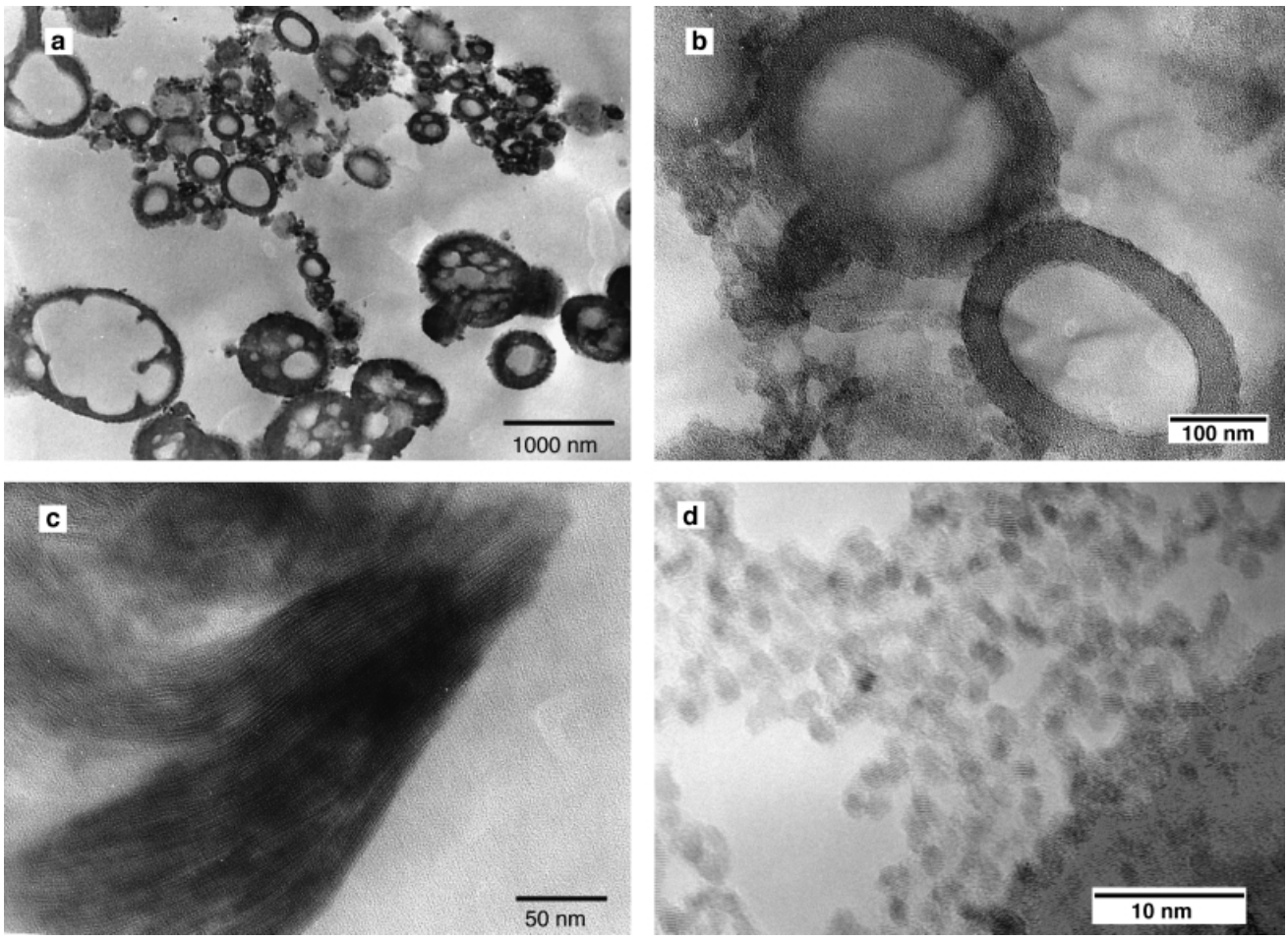

Figure 4. TEM images of molybdenum oxide bronzes a) at low magnification revealing the toroidal structures of approximately 300 nm in diameter including regions in which several smaller toroids have clustered together inside a larger toroid. These living-cell-like regions reorder into larger toroids upon exposure to the TEM electron beam, b) higher magnification reveals the mesostructured nature of the walls of the toroid. Scanning electron microscopy (SEM) revealed no salient structural features or tubular forms, which indicates that these toroids are relatively flat (ca. 50 nm). Other areas of sample exist in which there is no higher order to the mesostructured system, although the toroidal regions dominate the material, c) lamellar region of the mesostructured molybdenum oxide blue showing that certain regions of the bronze have reordered into a layered phase in the blue, d) close up of a region of the molybdenum blue showing where crystallization of the walls of the mesostructure into oxide grains approximately 1.5 nm in size has led to partial degradation of the occluded mesopores. Samples were prepared either by sonication in isopropanol or microtoming followed by deposition on a carbon-coated copper grid. Micrographs were recorded at 300 KV on a Hitachi H-9000 STE microscope.[52]

2.4. Photocatalytic Activity of Mesoporous Niobium and Phosphated Titanium Oxides

An important area of application of mesoporous transition metal oxides is in photocatalysis. In the past decade, a variety of photocatalytic systems centered around oxidative degeneration of organic chemicals,[56, 57] fixation of carbon dioxide,[58–60] evolution of H_2 from water,[61, 62] and the reduction of metal ions[63] were developed using semiconducting transition metal oxides. Coupling the controlled pore size and high surface areas of mesoporous materials with photocatalytic properties would thus represent an important advance. Titanium dioxide, because of its efficient electron-hole pair separation and low cost, is one of the most desirable materials for photocatalytic applications. In 1998 Stone and Davis studied the photocatalytic activity of phosphated titanium and niobium oxide based mesoporous molecular sieves.[64] The well-known oxidative dehydrogenation of 2-propanol to acetone was used as a probe to measure the photocatalytic activity of the materials. The quantum yields were defined as the molecules of acetone formed per incident photon (wavelength of light as incident light resource was about 360 nm). The surface areas, band gaps, and quantum yields of the phosphated titanium and niobium oxide catalysts are summarized in Table 2.

Table 2. Characterization and reactivity results for titanium and niobium materials.

Samples	Surface area [$m^2 g^{-1}$]	Band gap [eV]	Quantum yield ϕ
meso-TiO_2(473 K)[a]	712	3.19	0.0026
meso-TiO_2(973 K)[a]	90	3.25	0.0089
meso-TiO_2, extracted	603	3.15	0.010
ns-TiO_2, as-synthesized	–	3.24	0.0094
ns-TiO_2(873 K),[a] 1 h	39	–	0.022
ns-TiO_2(873 K),[a] 3 h	36	3.22	0.038
ns-TiO_2(873 K),[a] 12 h	28	3.26	0.27
Anatase (Aldrich)	9	3.28	0.41
Degussa P25	50	3.22	0.45
meso-Nb_2O_5	415	3.29	0.0041
Nb_2O_5	13	3.08	0.217

[a] The calcining temperature is given in parenthesis.

The lower photocatalytic activity of mesoporous titanium and niobium oxides compared to the anatase phase was attributed to the amorphous nature of the walls of these materials and the presence of phosphorous in the case of the titanium dioxide materials: the low degree of crystalline wall and the high surface concentration of defects lead to surface electron-hole recombination, and/or the poisoning of catalytic surface sites by the phosphorus remaining from the templates. Since high surface area mesoporous titanium dioxide is now readily available, the presence of phosphorous in these materials should no longer hinder applications,[36] although from these studies it appears that the low crystallinity of the walls of the structure may be a larger hurdle to overcome before the development of functional mesoporous titanium oxide photocatalysts can be realized.

2.5. Photocatalytic Activity of Mesoporous Tantalum Oxides

Takahara and Domen et al. recently reported the photocatalytic activity of mesoporous tantalum oxide.[65] These studies were undertaken because Ta-based mixed oxides are highly active in the overall decomposition of water under UV irradiation.[66–68] When as-synthesized tantalum oxide, prepared by the method of Antonelli and Ying, was used as a photocatalyst, H_2 evolved in a speed of 50 $\mu mol\,h^{-1}$. In contrast, the sample calcined at 600 K, after template removal by acid treatment and solvent extraction, showed higher photocatalytic activity and released both H_2 and O_2 in a stoichiometric ratio, even though a brief induction period was observed. The initial H_2 evolution was attributed to the decomposition reaction of the remaining surfactants and the stoichiometric evolution of H_2 and O_2 started after complete consumption of the surfactant template. A NiO loaded sample showed higher photocatalytic activity and shorter induction time than those samples without NiO because NiO can act as cocatalyst in the water decomposition reaction (Figure 5). The optimal NiO loading level for the overall water decomposition was found to be 4.0 wt%. The NiO loaded samples showed an important trend in increasing photocatalytic activity. These results are summarized in Table 3.

Mesoporous Ta_2O_5 samples showed better photocatalytic activity than the non-porous amorphous and crystallized samples because of its higher surface area which results in a higher NiO loading level. These high activities as compared to those reported above for titanium and niobium oxides[64] were explained by the different band gaps of the respective materials. The stable photocatalytic activity of pretreated mesoporous Ta_2O_5 with 4 wt% NiO continued for more than 200 hours although the first run exhibited somewhat higher activity. From these results it is evident that mesoporous Ta oxides are effective photocatalysts and for this reason may spur a great deal of research interest over the coming years.

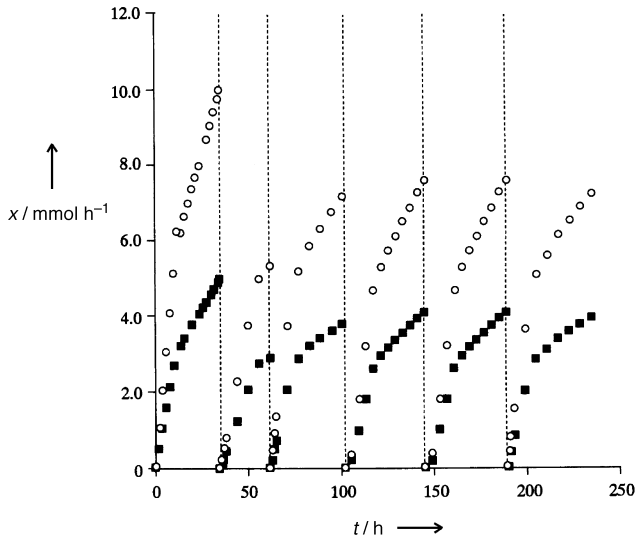

Figure 5. Time course of photocatalytic decomposition of water over NiO (4 wt%)-loaded mesoporous Ta_2O_5 after R673-0473 treatment: reduction at 673 K by H_2 followed by reoxidation in O_2 at 473 K. Reproduced with permission from ref. [65].

2.6. Alkali-Metal-Reduced Mesoporous Niobium, Tantalum, and Titanium Materials

Recent work in our group showed that mesoporous Nb, Ta, and Ti oxides can act as stoichiometric electron acceptors and hosts for a variety of electron-donating guest species, thus opening the doorway to a wide variety of reactions involving electron transfer to a mesoporous host lattice. This synthetic approach to achieving populated d states in the walls of the mesostructure differs appreciably from previous approaches in that the introduction of electrons into the d band occurs *after* the mesostructure has been formed. The use of air-sensitive, low-valent transition metal alkoxide precursors, which may well become oxidized during the course of mesostructure formation, can thus be avoided. In our work reduced transition metal molecular sieves[42] were obtained by

Table 3. Comparison of the photocatalytic activity of NiO loaded tantalum oxides.

Tantalum oxides	Loading of NiO [wt%]	BET surface area [$m^2 g^{-1}$]	H_2 produced [$\mu mol\,h^{-1}$]	O_2 produced [$\mu mol\,h^{-1}$]
amorphous Ta_2O_5[a]	1.0	145	46	24
treated[b]		NA	125	43
orthorhombic Ta_2O_5[a]	1.0	NA	10	0
treated[b]		NA	389	194
mesoporous Ta_2O_5[a]	4.0	370	150	73
treated[b]		141	515	272

[a] Crude material. [b] Calcinated template-free material.

treatment of mesoporous Nb oxide with Na/naphthalene in THF (Figure 6B). The reduced materials were gray to black and showed full retention of mesostructure after reduction as determined by XRD and nitrogen adsorption. The XPS spectra showed that the Nb $3d_{5/2}$, $3d_{3/2}$ emissions shift

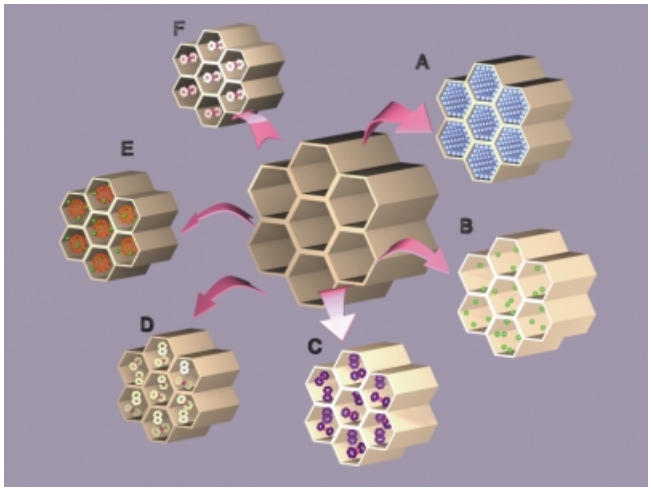

Figure 6. Reduction of mesoporous niobium oxide with: A) bis(toluene) niobium to give a material with low valent Nb on the surface; B) Sodium naphthalene to give a reduced sodium niobate with potential applications as a cathodic material; C) cobaltocene to give a material in which the mesostructure is filled with superparamagnetic molecular ensembles; D) nickelocene to give a mesoporous spin glass; E) K_3C_{60} to give one-dimensional potassium fulleride wires supported by the mesoporous oxide lattice; F) bis(benzene)chromium to give low-dimensional organometallic hole metals in the pores.

monotonically to lower binding energy with increasing reduction from 207.8, 210.6 eV for the unreduced materials to 206.0, 208.8 eV for the sample reduced with 1.0 equivalent of sodium naphthalene. This trend is consistent with a gradual change of the Nb oxidation state from Nb^V to Nb^{IV} as the Na loading level increases. However, the two distinct peaks for the Nb^{IV} and Nb^V were not resolved, possibly because of local electron hopping between sites faster than the XPS time scale. This work was then expanded to include all alkali-metal-reduced mesoporous Nb, Ta, and Ti oxides.[43] The order of stability to reduction by alkali metal was found to be Ta > Nb $\gg$ Ti as judged by retention of the XRD pattern after reaction. The band gaps for all materials studied ranged from 3.3–4.0 eV and the distance from impurity band, thought to be composed of the transition metal *n*d orbitals [$n = 3$(Ti), 4(Nb), 5(Ta)] and the alkali-metal *n*s orbitals [$n = 2$(Li), 3(Na), 4(K), 5(Rb), 6(Cs)], to conduction band was roughly 2.1 eV as calculated from their UV spectra (Figure 7). Interestingly, all of the alkali-metal-reduced Nb and Ta oxide materials studied were insulating (less than $10^{-8}\,\Omega^{-1}\,cm^{-1}$), while the Li–Ti material gave conductivity values of up to $10^{-6}\,\Omega^{-1}\,cm^{-1}$. The insulating nature of the Ta and Nb materials was attributed to Anderson localization effects, a phenomenon studied in Na-reduced amorphous tungsten oxides Na_xWO_3.[69] Since the Li–Ti materials are semiconducting, an Anderson transition to a more continuous electronic state may have occurred. The superconducting quantum interference device (SQUID) magnetometry mea-

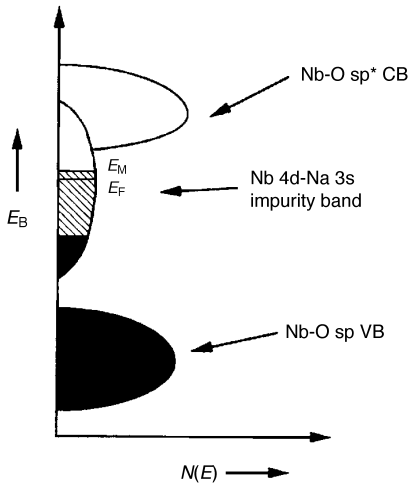

Figure 7. Energy-level diagram of alkali-metal-reduced M-TMS1 (M = Ta, Nb, Ti). The electron from the alkali metal resides in an *n*d(transition metal)-*n*s(alkali metal) impurity band between the valence and conduction bands of the mesostructure. E_f denotes the Fermi level while E_m represents the mobility edge. Black areas represent regions filled with electrons while the area marked by grid lines represents a region of localized states extending down into the (black) filled levels of the impurity band; CB = conduction band, VB = valence band. Reproduced with permission from ref. [43].

surement of all of these materials showed evidence for paramagnetic behavior. The presence of free electrons in the structure was further supported by their electron paramagnetic resonance (EPR) spectra showing one peak typical of a free electron (2.003 g). The electrochemical studies on the unreduced Ti materials give a cyclic voltammagram with two clear peaks at 0.8 V and 1.4 V, which indicate reversible reduction–oxidation of the oxide framework, and hence possible applications in Li batteries. The stoichiometric retention of reductant with almost no loss of porosity gives these oxides a distinct advantage over other porous cathodic materials, which typically undergo a phase change to a non-porous state on addition of more than just a few tenths of an equivalent of alkali metal.[70] This improvement is most likely to be the result the greater structural flexibility of the amorphous walls of mesoporous oxides as compared to the more rigid crystalline framework of other cathodic materials. In contrast, the unreduced Nb and Ta materials displayed very weak or no reversible electrochemical reduction–oxidation properties. The strong capacitance in these materials was attributed to charge mobility problems arising from greater electron localization in the Nb and Ta materials than in the Ti materials.

2.7. Superparamagnetic Mesoporous Niobium Oxide/Cobaltocene and Nickelocene Composites

Of special interest is the intercalation of cobaltocene into mesoporous niobium oxide.[71, 72] Cobaltocene is a strong reductant and has a rich host–guest inclusion chemistry with many layered materials, such as sulfides and selenides, that can act as electron acceptors.[73] Recent work in our group shows that mesoporous Nb oxide readily reacts with cobalt-

ocene to give a dark gray material (Figure 6C) which on increased cobaltocene loading undergoes a dramatic change in magnetic properties from paramagnetic to superparamagnetic behavior, a property which is normally only observed in the nanometer colloid grains of transition metals and their compounds. Interestingly, bulk Nb_2O_5 does not react with cobaltocene, which demonstrates that the broader distribution of energy of the d band in the amorphous mesostructure leads to a fraction of states which are low enough in energy to accept an electron from cobaltocene. The materials were characterized by XPS, and displayed Nb $3d_{5/2}$, $3d_{3/2}$ emissions at 206.8 and 209.6 eV, indicative of slight reduction from Nb^V to Nb^{IV} state as compared to the starting materials (207.6 and 210.4 eV), and the Co $2p_{3/2}$ region in the sample prepared with more than 0.5 equivalent of cobaltocene showed two distinct cobalt peaks for cobaltocene and cobaltocinium at 779.7 and 781.1 eV, respectively. The superparamagnetic materials have a Co/Nb molar ratio above a critical value of 0.5:1.0 and SQUID χ versus T measurements show a blocking temperature (T_b) of 18 K (Figure 8, curve a), below which the

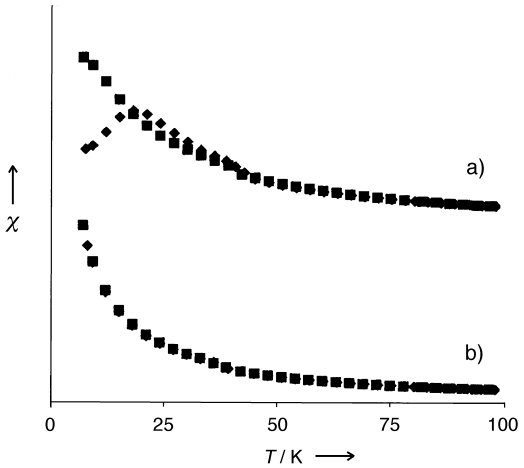

Figure 8. Temperature dependence of magnetic susceptibility for Nb-TMS sample (◆ = zero-field cooled with increasing temperature ■ = with reducing temperature) with a) 0.5 equivalents of cobaltocene showing a superparamagnetic blocking transition (T_b) at 22 K; b) 0.4 equivalents of cobaltocene showing no evidence of a superparamagnetic transition.

individual spins in the nanoscale magnetic domains are said to be blocked to certain low-energy transitions because of thermal fluctuations.[74] Materials with less cobaltocene were paramagnetic (Figure 8, curve b). The retention of neutral cobaltocene in the structure after the maximum level of cobaltocinium was reached was attributed to a strong host–guest interaction. This was the first reported example of superparamagnetism in a molecular ensemble.

Recently superparamagnetism was also observed in iron oxide based mesostructured surfactant composites,[75, 76] and it was attributed to small domains in the walls of the structure, not altogether surprising given that colloidal grains of many Fe-containing materials often display superparamagnetic properties. Since other reduced mesoporous oxides are not superparamagnetic, the origin of cooperative magnetism in this system must be related to the cobaltocene in the pores and short-range coupling between the unpaired electrons associated with the Co centers. Whether or not the unpaired electrons in the walls of the structure interact with the spins of the Co species is not know at this stage. What makes this system particularly unusual is that bulk cobaltocene is paramagnetic and superparamagnetism is normally observed in small grains of materials which are ferromagnetic in their bulk form.

To investigate the factors contributing to superparamagnetism in this system, a study of variation of pore size, pore wall thickness, and wall composition was conducted.[72] The wall thickness and pore sizes were systematically varied from 15–30 Å and the 23-33 Å, respectively, while the composition of the walls was varied from Nb, to Ta, and Ti. SQUID measurements, χ versus T and B versus H, were performed for all the materials. In all the materials the mean particle size was estimated from the magnetic data to be about 14 nm.[77] The pore size and wall thickness of the mesostructure seemed to have little effect on the magnetic behavior of these materials. The presence of cigar-shaped cobaltocene-based clusters within a single pore rather than spherical regions spanning several pore diameters was invoked to explain the 14 nm domain sizes, since some effect on the magnetic properties of increasing pore-wall thickness would be expected if the pore walls were part of the magnetic domains. The samples synthesized from cobaltocene and Ta-TMS1 or Ti-TMS1 absorbed much lower levels of organometallic reagent, mostly in the nonmagnetic cobaltocinium ion form, and only displayed paramagnetic behavior. The lower levels of cobaltocene absorbsion were attributed to the lower oxidizing ability of the walls of these materials as compared to the Nb-based structures. Thus, from this study, it is evident that the host material must be reactive enough towards reduction by a guest species to absorb, in a first step, a critical amount of cobaltocene in the cobaltocinium ion form. Once this critical level has been reached the materials absorb more cobaltocene, but this time in the neutral form. Once enough cobaltocene has aggregated in the pores, the materials undergo a transition to superparamagnetic behavior because of an increased density of unpaired electrons in the pore channels.

To investigate the effect of the overall spin of the guest species on the magnetic behavior of the system, we chose to synthesize mesoporous niobium oxide composites of metallocene species with more than one unpaired electron per nucleus.[78] Thus, new composite materials were prepared from nickelocene, which has two unpaired electrons per Ni center, and mesoporous niobium oxide (Figure 6D). These materials showed an interesting loading-dependent transition from superparamagnetic (blocking temperature T_b at 8 K) to spin-glass behavior, a phenomenon normally associated with amorphous metal alloys in which the spins essentially become "frozen" in a random orientation below a certain temperature. These nickel-based composites in general possessed a much lower loading level of organometallic species, as determined by XPS (molar ratio of Ni:Nb was 0.07:1), than the cobalt-based composites. This result was rationalized by the greater number of unpaired electrons in Ni-based materials, that is, the ground state of nickelocene is a triplet

state and its cation is in a doublet state while cobaltocene is in a doublet state and its cation in a singlet state. In a study of magnetic behavior of Fe-doped Pd alloys, a transition from the superparamagnetic state to the spin-glass state was found to occur on increasing the concentration of the magnetically active species in the alloy.[79] The transition to the spin-glass state in the nickelocene composites took place at the molar ratio of Ni:Nb in the amount of 0.1:1. Currently we are embarking on a series of more detailed magnetic studies in an effort to elucidate the origin of superparamagnetism and spin-glass behavior in this new family of reduced mesoporous composites.

2.8. Low-Dimensional Organometallic Molecular Wires Supported by a Mesoporous Niobium Oxide Host

While late transition metal sandwich complexes form insulating materials with magnetic properties typical of fine particles and amorphous alloys, the analogous early transition metal species ($[Cp_2Cr]$, $[Cp_2V]$, $([C_6H_6)_2Cr]$, $[(C_6H_6)_2V]$; $Cp = C_5H_5$) generally form paramagnetic materials (Figure 6F) with conductivity values as high as $10^{-5}\ \Omega^{-1}\,cm^{-1}$.[80] In these composites, the retention of the mesostructure after all reactions was confirmed by the powder XRD patterns and nitrogen adsorption–desorption isotherms. In the $[(C_6H_6)_2Cr]$ system, both $[(C_6H_6)_2Cr]$ and $[(C_6H_6)_2Cr]^+$ were detected in the pores by XPS and ESR. The Nb oxide walls of the mesostructure showed signs of very slight reduction, consistent with electron transfer from the organometallic species to the host lattice. The conductivity in the Cr- and V-based materials was rationalized by a model where the hole in the mixed oxidation state organometallic phase (introduced by oxidation by the mesostructure) is the charge carrier, since in all the cases studied both cationic and neutral species were required for conductivity, and the reduced mesostructure was previously shown to be insulating. To study the effect of changing the dopant on the conductivity of this new family of materials, bis(benzene)vanadium, vanadocene, and chromocene composites of mesoporous niobium oxide were prepared.[81] The conductivity of these materials was 10^{-4}, 10^{-5}, and $10^{-6}\ \Omega^{-1}\,cm^{-1}$, respectively. The mixed oxidation states nature of the organometallic phase in each material was revealed by XPS and EPR which provided concrete evidence for $[(C_6H_6)_2V]/[(C_6H_6)_2V]^+$, $[Cp_2V]/[Cp_2V]^{2+}$, and $[Cp_2Cr]/[Cp_2Cr]^+$ in the pores of the respective materials, however, all in levels of less than 0.01 equivalents of total dopant per mole of Nb, almost 50 times less than that in the cobaltocene system, which was completely insulating under the conditions studied. These trends were rationalized by the balance between Hubbard potentials U and bandwidths W of the transition metals in question where the hole in the mixed-oxidation-state phase was regarded as the charge carrier in each system.[82] Currently we are performing solid-state NMR spectroscopy and variable temperature conductivity studies on these materials to further elucidate their structure and properties. Recent unpublished results in our group have demonstrated that bis(toluene)niobium acts as an Nb transfer reagent, effectively depositing Nb atoms on the surface of the mesostructure.[83] In this case a mixed-valent organometallic phase it not formed, presumably because of the instability of the bis(toluene)niobium cation. We are currently investigating the physical properties of this new composite.

2.9. One-Dimensional Alkali-Metal Fulleride Wires Supported by a Mesoporous Niobium oxide Host

Another family of electroactive mesoporous transition metal oxide materials recently reported by our group are the mesoporous niobium oxide intercalates of the superconductor K_3C_{60} (Figure 6E).[84, 85] Since the electronic properties of alkali-metal fullerides show a strong dependence on the level of reduction,[86] an important aspect is that the oxidation state of the fulleride phase in the pores can be easily tuned by the addition of potassium naphthalene. The pore size of the mesoporous niobium oxide host material used in this study was 22 Å, just large enough to accommodate one molecule of K_3C_{60} (unit-cell length ca. 14 Å) across the diameter of the pore. This feature allows us to investigate the properties of one-dimensional alkali-metal fullerides and the effects of quantum confinement on superconductivity and metallic properties of alkali-metal fullerides in general. The reaction of K_3C_{60} and trimethylsilylated mesoporous niobium oxide in THF solution gave a material with alkali-metal fulleride with an oxidation state of $n = 0.5$ in the pores, as measured by its Raman spectra (for fulleride salts of the type M_nC_{60} (M = K, Rb, Cs), the A_g mode shifts roughly 6 cm^{-1} for every integer increment in the value of n).[86] The reduction of the niobium mesostructure by the fulleride was illustrated by XPS spectrum, which indicated a level of reduction equivalent to that obtained by treatment of mesoporous niobium oxide with 0.4 equivalents of potassium naphthalene. The conductivity of this material was $1.25 \times 10^{-3}\ \Omega^{-1}\,cm^{-1}$, several orders of magnitude greater than that observed for a sample of fulleride-free mesoporous niobium oxide reduced with 0.4 equivalents of potassium naphthalene. This result suggests that the conductivity pathway in this material is through the fulleride-units on the surface of the material or through the channels, and not through the niobium oxide walls of the structure. When this composite was further reduced by potassium naphthalene back to $n = 3$ state, the conductivity of this new material was lower than $10^{-7}\ \Omega^{-1}\,cm^{-1}$. No further reduction of niobium oxide walls of the mesostructure was observed in this process. Neither material showed signs of a T_C that might indicate a transition to superconducting behavior, which is not altogether unexpected given the strong dependence of superconductivity on structure in solids. EPR studies suggest that the fulleride phase and the free electron in the walls of the mesostructure are behaving as isolated systems. The room-temperature conductivity patterns of these materials confirm calculations that K_3C_{60} should be a Mott–Hubbard insulator because of its half-filled t_{1u} band[86] and that the accidental vacancies in the $n = 3$ state are responsible for the metallic behavior of bulk K_3C_{60}. However, more structural information is necessary before any direct comparisons can be made to the bulk state.

To more fully probe the dependence of room-temperature conductivity on oxidation state of the fulleride in the pores, the parent composite with $n = 0.5$ was reduced in small increments up to $n = 4.5$, the process was monitored by Raman and XPS. Interestingly, two conductivity maxima at $n = 2.6$ and 4.1 were revealed in this system.[87] The conductivity of the materials at these two states was 10^{-4} and $10^{-1}\ \Omega^{-1}\,cm^{-1}$, respectively. The maximum at $n = 2.6$ provides indirect evidence that the potassium fulleride phases other than $n = 3$ state might be involved in the conductivity in bulk K_3C_{60}. The maximum at $n = 4.1$ is perhaps even more surprising since the room-temperature conductivity of this composite is almost as high as pure K_3C_{60} and the $n = 4$ state is thought to be insulating.

The effects of pore size and wall composition of mesoporous transition metal oxides on the conductivity of the composites were also studied by changing the mesostructure hosts from Nb to Ti and Ta and expanding the pore size to 32 Å, large enough to accommodate two unit cells across a pore rather than only one. The results revealed that the double maximum behavior was general to other porous hosts, however, the differences in the positions of the maxima were too subtle to draw any conclusions. The change in pore size seemed to have little effect, which suggests that a much more dramatic change in pore size might be necessary to affect the electronic properties. An interesting trend that emerged, however, was an increase in the density of states near the Fermi level, as measured by XPS, in all the samples at the transition point to the conductivity maximum at $n \approx 4.0$. This observation is consistent with a transition to metallic behavior, possibly involving a favorable overlap between the band structure of the walls and the fulleride phase, although we are currently performing variable-temperature resistivity studies to confirm this hypothesis.

2.10. Electroactive Mesoporous Tungsten Oxides

Cheng and co-workers recently reported the syntheses and electrochromic properties of mesoporous tungsten oxide films.[88] These materials were prepared by dip-coating using block copolymers as templates, a procedure that was developed by Stucky's group.[89, 90] The coating solutions consisted of a mixture of WCl_6, anhydrous ethanol, and tri-block polymer $EO_{20}PO_{70}EO_{20}$ (BASF Pluronic P_{123}), and either solvent extraction or calcination was used to remove the copolymer template. These materials were characterized by thermogravimetric analysis (TGA), XRD, TEM, and nitrogen adsorption–desorption, which gave compositions of $WO_{2.94} \cdot 2.8\,H_2O \cdot 0.011\,P_{123}$, $WO_{2.94} \cdot 1.3\,H_2O \cdot 0.001\,P_{123}$, $WO_{2.94} \cdot 0.8\,H_2O \cdot 0.0005\,P_{123}$, and $WO_{2.97} \cdot 0.17\,H_2O$ for the as-synthesized, solvent extracted, 300 °C calcined, and 400 °C calcined samples, respectively. The mesostructures possessed fairly regular pore diameters but were not well ordered and generally collapsed at 400 °C during calcination. The BET surface area for the solvent extracted and calcined (300 °C) samples were 155 and $135\ m^2 g^{-1}$, respectively, and the corresponding average pore sizes were 50 and 45 Å.

Voltammetric measurements of the mesoporous tungsten oxide films showed a well-defined anodic peak for the samples calcined at 300 °C and 400 °C and well-behaved electrochemical reversibility after several cycles. The cyclic voltammagrams of samples calcined at 300 °C showed the evolution of multiple anodic peaks during the repetitive insertion–desertion scans which could arise from the different types of hydrogen injection sites and/or the high surface area of the films.

The electrochromic properties of mesoporous tungsten oxide were also studied. The optical change observed for the sample calcined at 300 °C, or for a sample extracted by ethanol during the voltammetric sweep, was completely reversible (Figure 9), while tungsten oxide samples with low surface

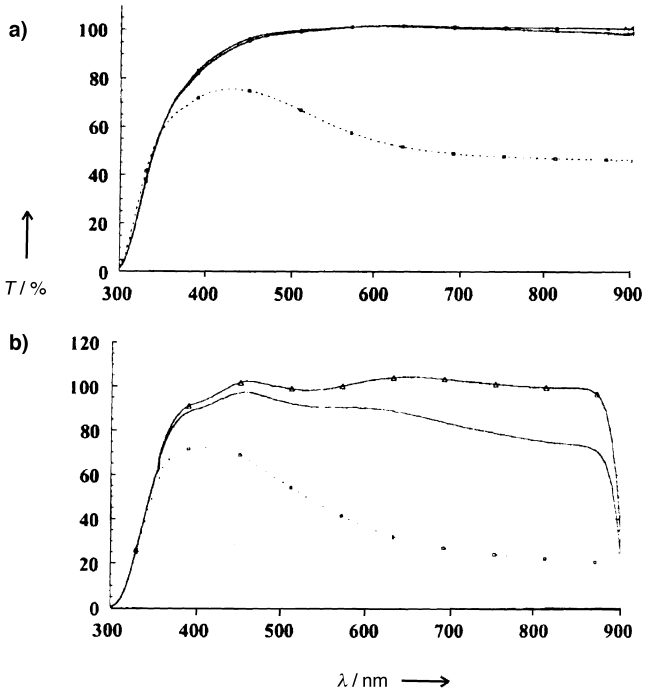

Figure 9. Optical transmittance spectra for a) mesoporous and b) sol–gel tungsten oxide films heated at 300 K. △ = initial; —— = +0.8 V (1st charge); •••• = −0.8 V (1st discharge). Reproduced with permission from ref. [88].

areas, such as a sol–gel derived non-mesoporous film heated at 300 °C, and the same sample heated at 400 °C showed an irreversible coloration/bleaching process. This result was further confirmed by the plots of transmittance variation at 650 nm as a function of time, the data were obtained for the transient absorption response to the voltage step. The coloration efficiency (CE) for mesoporous tungsten oxide film calcined at 300 °C was $21.2\ cm^2 C^{-1}$ for the first cycle. The chromoamperometric measurements for voltage steps between −0.8 V and +0.8 V (vs. SCE (saturated calomel electrode)) showed the mesoporous films possess better electrochemical stability than the sol–gel nonporous film. Therefore, the high surface area resulting from the mesoporosity of the tungsten oxide films provides enhanced electrochemical and electrochromic properties.

3. Mesostructured Sulfides and Selenides

3.1. Mesostructured Germanium Sulfides

Because of their anticipated electronic and optical properties and affinities for heavy metals, researchers have recently been investigating the synthesis and potential applications of mesostructured sulfides and selenides. Ozin's group recently reported a new family of surfactant-templated metal germanium sulfide materials with structures similar to that of as-synthesized MCM-41.[41, 91] Various groups have reported mesostructured chalcogenide composites, such as CdS,[92–94] ZnS,[95] SnS_2,[96] GeS_2,[97] and CdSe.[98] The representative synthetic strategy was developed by Stupp and co-workers. This method involves passing H_2S or H_2Se over a hexagonal mesophase containing the ether $C_{18}H_{35}(OCH_2CH_2)_{10}OH$, water, and Cd^{II} or Zn^{II} salts. In contrast, the mesostructured metal germanium sulfides synthesized in Ozin's group were prepared by a non-aqueous surfactant-templating assembly of adamantanoid $[Ge_4S_{10}]^{4-}$ cluster precursors in formamide, where $(TMA)_4Ge_4S_{10}$ (TMA = tetramethylammonium) was used as the inorganic precursor and $C_nH_{2n+1}NMe_3^+X^-$ ($n = 12$, 14, 16, 18, and $X = Cl^-$, Br^-) were used as structure-directing agents (Figure 10). Transition metal cations such as Co^{2+}, Ni^{2+}, Zn^{2+}, or Cu^+ were employed as charge-balancing and inorganic framework-chain-linking ions to create well-ordered hexagonal mesostructures.

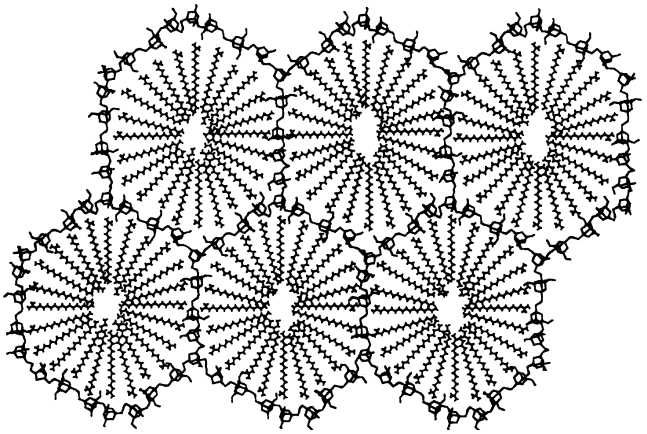

Figure 10. Proposed architecture of a mesostructured germanium sulfide material. $(TMA)_4[Ge_4S_{10}]$ and (CTA)Br were dissolved in formamide to give a viscous mesophase of the adamantoid clusters charge balanced by surfactant. On addition of a metal salt, the adamantoid clusters link to form a supramolecular, hexagonal, mesostructured material in which the adamantoid clusters are linked by metal ions in the structure.

The powder XRD patterns and TEM images of these materials illustrated a moderate degree of mesostructural order with wormlike morphologies and hexagonal unit cells (Figure 11). The Raman spectra of the mesostructured materials showed overlapping peaks between 240 and 320 cm^{-1} for the Zn–S stretching modes, which confirms the presence of metal-linked adamantanoid clusters in the material. The solid-state ^1H (MAS) NMR spectra and cross-polarization (CP) ^{13}C (MAS) NMR spectra confirmed the presence of the surfactant in the materials, as did TGA and

Figure 11. TEM images of wormlike particles of $(CTA)NiGe_4S_{10}$. A magnified view of the particle in (right) confirmed that the channels of the material run parallel to the longitudinal axis of the faceted shape. Reproduced with permission from ref. [91].

pyrolysis mass spectrometry. No sulfur-containing small molecules, such as H_2S, HSMe, and Me_2S, were detected in the mass spectra. The elemental analyses gave $(CTA)_2M_2Ge_4S_{10}$ with 3–10 wt% unaccounted mass for most of the samples. Only 40% of the surfactant in the materials could be removed by acetone extraction, which indicates that the cationic surfactants (CTA) were functioning as charge-balancing reagents for the anionic framework as well as space-fillers to reinforce the mesostructure. A liquid-crystal templating mechanism was proposed to rationalize the formation of these materials. In this mechanism the terminal negative sulfide groups of the admantanoid clusters in the initially formed micellar and cylindrical liquid crystalline phase by $[Ge_4S_{10}]^{4-}$, TMA^+, and surfactant cations could rapidly coordinate to the transition metal species to form a hexagonal mesostructured network. Because of the well-defined nature of the crystalline units in the walls of these materials, it is anticipated that numerous electronic and optical applications, in which a well-defined wall-structure is an advantage, may be possible.

3.2. More Germanium Sulfides and Selenides and Even Some Tin

At about the same time the non-aqueous synthesis of mesostructured metal germanium sulfides from $[Ge_4S_{10}]^{4-}$ clusters was being developed by Ozin's group, Kanatzidis and co-workers were working on the synthesis of related mesostructured metal germanium sulfides and selenides, $(C_nH_{2n+1}NMe_3)_2[MGe_4Q_{10}]$, where Q = S and Se, M = Zn, Cd, Hg, Ni, and Co, $n = 12$, 14, 16, 18,[40, 99] using a mainly aqueous route (with a small amount of ethanol and methanol). Certain aspects of the synthetic method, chemical formula, overall three-dimensional framework organization, and thermal stability of the materials are different from those reported by the Ozin group. The method developed by Kanatzidis and co-workers involves the stoichiometric metathesis reactions between $[Ge_4Q_{10}]^{4-}$ (Q = S, Se) anions and metal dichlorides in the presence of long-chain cationic surfactants at 20–80 °C. The charge on the $[Ge_4Q_{10}]^{4-}$ cluster was balanced by one M^{2+} and two surfactant $RNMe_3^+$ ions. Energy dispersive microprobe analysis (EDS) on the resulting material gave the chemical formula $(RNMe_3)_2[MGe_4Q_{10}]$, slightly different from the formula of the materials synthesized by the Ozin group.[41] The powder XRD patterns, high resolution (HR) TEM images and atom pair distribution function (PDF) plots of these materials revealed a mesostruc-

tured nature with short-range local order and nonperiodic disordered wall structure much like that of mesoporous silica MSU-1, MSU 2, and MSU 3.[100] The surfactant-filled inorganic framework pores were composed of adamantanoid $[Ge_4Q_{10}]^{4-}$ clusters with linking tetrahedral divalent transition metal ions, and organized in a worm-hole pattern with a constant average tunnel to tunnel distance (Figure 12). The pore size could be tuned from 30 to 45 Å by varying the

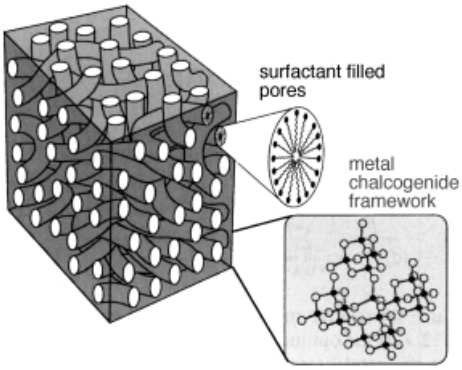

Figure 12. Proposed structure model of the C_nMGeQ phases. The amorphous framework is perforated by the wormhole-like micelles of surfactant molecules.

surfactant chain length and the overall structure of the $[MGe_4Q_{10}]^{2-}$ framework. The Raman and IR spectra of these materials showed that the adamantanoid clusters remained intact and gave evidence for additional M–Q bonds present. All materials were wide band gap semiconductors in the energy range of 1.0–3.6 eV and the band gaps were independent of the surfactant chain length. Based on the TGA, about 70–80 % of surfactant inside the inorganic framework could be removed without collapse of the mesostructure by heating at about 180–220 °C under vacuum for 3–4 days.

Materials containing the divalent Mn^{2+} ion behaved differently and did not lead to an immediate precipitation in either the non-aqueous or aqueous mediums described above. This problem was resolved by conducting the reaction of $Na_4Ge_4S_{10}$, $MnCl_2$, and mesityltrimethyl ammonium bromide in a stoichiometric ratio under hydrothermal conditions.[101] This method resulted in new hexagonally ordered mesostructures of metal germanium sulfides with only short-range local order similar to those reported by Ozin's group. The semiconducting properties of this material were confirmed by solid-sate absorption spectra, giving a band gap of 2.84 eV.

Trivalent cations, such as Ga^{3+} and In^{3+}, can also act as the cluster-linking agents in these materials, which leads to light-emitting mesostructured sulfides with hexagonal order.[102] The mesostructure of these two materials were similar to their divalent counterparts and the optical absorption confirmed their semiconducting behavior. The chemical formula of both materials was close to $(CP)_2M_{1.3}Ge_4S_{11}$ (CP = cetylpyridinium, M = Ga^{3+}, In^{3+}), indicative of a very high metal content which could not be accounted for by the charge balance between surfactant, metal cations, and cluster anions, possibly because of the presence of S^{2-} species. A unique feature of these two materials was the intense photoluminescence observed when excited with light energy above their band gaps. For example, under an excitation light of 3.35 eV (370 nm) at 77 K, an intense green emission with a maximum 2.35 eV (528 nm) and 2.32 eV (535 nm) was observed for CPGaGeS and CPInGeS, respectively (Figure 13). The optoelectronic property possibly originates from the pyridinium chromophore of the surfactant. This was the first observation of light emission from mesostructured metal thiogermanates.

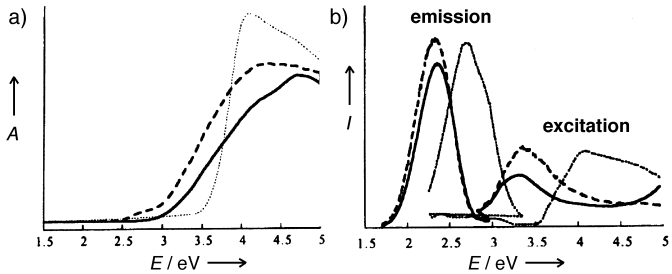

Figure 13. a) Electronic absorption spectra of mesostructured sulfides. b) Photoluminescence and excitation spectra of the same materials (——: CPGaGeS; – – –: CPInGeS; ••••: CPBr). Reproduced with permission from ref. [102].

This methodology of supramolecular assembly of chalcogenide nanocomposites could be expanded to synthesize stable binary systems including $[Fe_4S_4]$ and $[Ge_4Q_{10}]^{4-}$ (Q = S, Se) clusters as building blocks for the inorganic frameworks.[103] The cluster $[Fe_4S_4]$ was selected as a research target because it is important in biological systems, and provides a major part of the foundation for electron transfer, catalytic, and enzymatic processes in living organisms.[104] This material possessed hexagonal mesoscopic order and was prepared in the non-aqueous solvent mixture of formamide and dimethyl formamide (DMF). This general method has opened a doorway for preparing a stable hybrid system with multiple functionality.

Another new class of mesostructured selenide semiconductors with an open framework based on tetrahedral $[SnSe_4]^{4-}$ ion was reported recently by the Kanatzidis group.[105] These materials are important not only because of their interesting electronic properties but also because of their varied pore organization, which includes disordered worm-hole, hexagonal, and even cubic phases. It was known that $[SnSe_4]^{4-}$ possessed the same tetrahedral structure as $[SiO_4]^{4-}$ and that it was smaller and heavier than the $[Ge_4Q_{10}]^{4-}$ (Q = S, Se) clusters. Therefore, it was expected that a similar topological structure to silicas and semiconductors with narrower band gaps than metal germanium chalcogenides would be obtained. These materials were made by spatially controlled assembly of $[SnSe_4]^{4-}$ ions in formamide with various divalent metals such as Mn^{2+}, Fe^{2+}, Co^{2+}, Zn^{2+}, Cd^{2+}, and Hg^{2+} in the presence of cetylpyridinium surfactant as the template. Their general chemical formula were described as $(CP)_{4-2x}M_xSnSe_4$ (where $1.0 < x < 1.3$). XRD patterns and TEM images revealed that, under the same experimental conditions, all the materials had hexagonal mesostructures such as silica MCM-41 except the Zn analogue, which had a cubic mesostructure such as MCM-48. The structure of the Zn materials was dependent on the surfactant concentration. When the concentration was reduced by 50 %, the product had an hexagonally ordered

mesophase with uniform pore size. The presence of the tetrahedral $[SnSe_4]^{4-}$ ion clusters was demonstrated by ^{119}Sn Mössbauer spectroscopy. The UV-visible/near-IR spectroscopy showed the band-gap transition in the energy range of 1.4 – 2.4 eV, values similar to those of CdTe (1.45 eV) and GaAs (1.54 eV) semiconductors. In summary, while these materials are not yet completely stable to template removal, their fascinating array of ordered structures and unusual opto-electronic properties may lead to applications in which accessible internal void-space porosity is not a requirement.

4. Mesostructured Metals

4.1. Mesostructured Platinum

Because of the importance of zero-valent transition metals in many catalytic processes the synthesis of nanostructured metals with high surface areas and controlled porosity represents a significant challenge for materials scientists. In 1997 Attard and co-workers reported the aqueous syntheses of mesostructured metallic platinum by surfactant liquid crystal templating.[106] In this work, hexachloroplatinum acid (H_2PtCl_6) and ammonium tetrachloroplatinate $[(NH_4)_2PtCl_4]$ were employed as the metal source and octaethyleneglycol monohexadecyl ether $C_{16}(EO)_8$ as the hexagonal structure-directing agent. To obtain mesostructured platinum metal, pure Fe, Zn, Hg, or hydrazine hydrate, were used in situ as reducing agents after the self-assembly processes for the system H_2PtCl_6 and $[(NH_4)_2PtCl_4]$, respectively. The surfactant template, metal residues, and small molecules were removed by repetitive washes with acetone, water, and hydrochloric acid until TGA showed almost no further weight loss at up to 600 °C in air. SEM images revealed that the materials were composed of particles 90 – 500 nm in diameter, and TEM showed evidence of small grains possessing a hexagonal mesostructure with a pore diameter of 30 Å and a pore wall thickness of 30 Å (Figure 14). These results were consistent with the broad and poorly defined XRD pattern, indicative of either small domains of hexagonal order or large amorphous regions in the sample. The extended X-ray absorption fine structure (EXAFS) data obtained for the platinum L_{III} edge of the materials were in good agreement with the presence of pure platinum metal and no oxygen backscattering shells were found. The amplitude of the EXAFS spectrum and the corresponding coordination number of mesoporous platinum were lower than those of bulk metallic platinum (also revealed by EXAFS) could be attributed to high surface area for the mesoporous materials, although no nitrogen adsorption data was reported. In a subsequent paper, this technique was extended to the synthesis of thin films,[107] and nitrogen adsorption studies revealed surface areas of 23 $m^2 g^{-1}$, comparable to that of colloidal Pt. The proposed mechanism of mesostructure formation in this new class of materials involved stabilized metal precursors at the interface between the hydrophobic and hydrophilic domains of the microphase-separated environment. Then the fast reduction of the platinum salts yielded small colloidal primary metallic particles on the interface followed by agglomeration and coalescence until the walls become homogeneous. This interesting new method has recently been extended to liquid crystal template syntheses of Ru/Pt alloys[108] and shows promise as a general method towards mesostructured metallic materials which may find applications in catalytic hydrogenation and fuel-cell design.

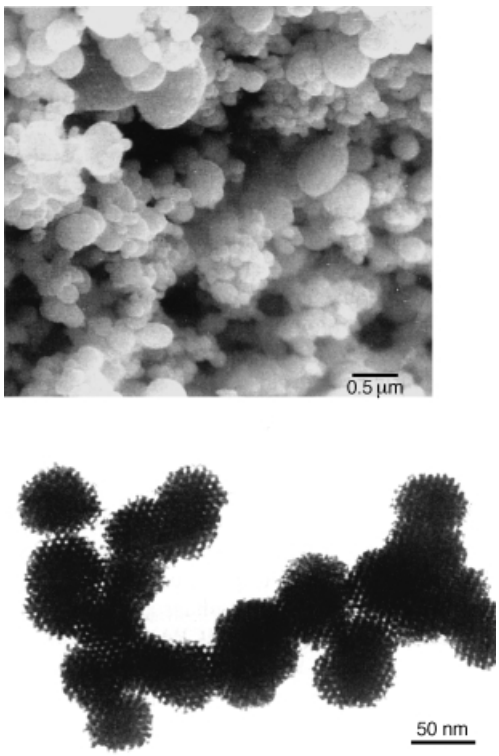

Figure 14. SEM image of a washed sample of mesoporous platinum (top) and TEM image of H_I-platinum (bottom). The material was suspended in acetone, sonicated for 5 min. and applied to a carbon-coated copper grid.[106]

4.2. Metal Carbonyl Compounds as Mesostructure Building Blocks

In 1998, we attempted the synthesis of mesoporous Pt using metal carbonyl anions and cationic surfactants as building blocks with thermal or photolytic decomposition of the resulting self-assembled platinum carbonyl surfactant phases required to eliminate the carbon monoxide and leave behind the pure metal mesostructure.[109] While this work resulted only in the formation of layered phases, it is included in this review because of the novelty and potential promise of this new synthetic method. Ionic metal carbonyl clusters ($Na_2[PT_A(CO)_6]_n$, $n = 3-5$) were selected as building blocks because of the great flexibility of composition, size, average charge per Pt atom, and the relative ease of thermal decomposition to the pure metallic state. Trimethyl ammonium surfactants were employed as structure directing agents (Figure 15).

The interdigitated layered structure of these materials was revealed by XRD. The layered structure was further confirmed by TEM images, which showed small regions of local order. Changes in the metal-to-surfactant ratio, brought about

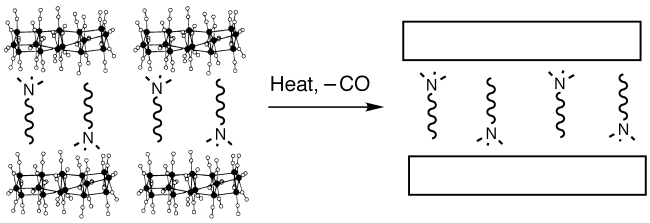

Figure 15. Thermal treatment of layered platinum carbonyl phases results in loss of CO and formation of a new platinum-based layered material.[109]

by simply changing the size of the metal carbonyl cluster, or precipitation directly from cold methanol without the addition of degassed water, had no effect on changing the nature of the layered mesophase. Thus no hexagonal or cubic phases were observed. Elimination of CO from the as-synthesized materials by heating at 70 °C under dynamic vacuum resulted in the retention of the structure with only a slight shrinkage of the interlayer spacing with $d(100)$ going from 19.6 Å to 19.1 Å. The lack of regularly spaced gaps between the platinum units within each layer suggested that the individual platinum clusters had condensed together or that the gaps were too small to be observed. The elemental analyses and ^{13}C (MAS) NMR spectra confirmed the presence of surfactant in this material. No platinum oxide was observed by energy dispersive X-ray spectra (EDS). Further heating of this material at 120 °C for two days led to loss of the layered structure and formation of an amorphous phase. While only layered materials were formed, this study demonstrated that metal carbonyl anions could be used as precursors to pseudo metallic phases, the loss of CO and condensation of the walls on thermal or photolytic treatment being related to the loss of water and formation of metal – oxygen bridges in the sol – gel synthesis of metal oxides.

5. Summary and Outlook

From the contents of this review it is clear that the area of mesoporous non-silica materials has expanded significantly in the last several years and that real-world applications of these exciting materials may not be too far off. By offering controlled porosity, large accessible internal surface areas and void space, in combination with the variable oxidation states of transition metals or semiconducting behavior of sulfides and selenides, this class of materials possess many crucial properties that hitherto have not been possible in zeolites or mesoporous silicates. Already functional materials in this class have been developed for use in photocatalysis, fuel cells, catalytic oxidation, and reduction, while many other applications are no doubt forthcoming. Moreover, the propensity for mesoporous transition metal oxides to act as stoichiometric electron acceptors, which makes them obvious candidates for cathodic materials, has allowed for the exploration of new one-dimensional hole-doped molecular metals with unusual electronic and magnetic properties not observed in the bulk state of these materials, while the opto-electronic activity of narrow band gap selenides and sulfides may lead to development of improved materials for light-harvesting devices. Since this area of porous materials is still in its infancy it is clear that we are only witnessing the beginning of what has already developed into one of the most active and exciting areas of materials science.

The Ontario Premier's Research Excellence Award program, NSERC, and The Petroleum Research Fund are acknowledged for financial support. Viktoria Mouratova is thanked for her artistic contributions.

Received: July 2, 2001 [A 481]

[1] O. G. Schmidt, N. Schmarje, C. Deneke, C. Müller, N.-Y. Jin-Phillipp, *Adv. Mater.* **2001**, *13*, 756 – 759.
[2] M. J. Whitcombe, E. N. Vulfson, *Adv. Mater.* **2001**, *13*, 467 – 478.
[3] K. Y. Lee, M. C. Peters, D. J. Mooney, *Adv. Mater.* **2001**, *13*, 837 – 839.
[4] T. Q. Nguyen, J. Wu, S. H. Tolbert, B. J. Schwartz, *Adv. Mater.* **2001**, *13*, 609 – 611.
[5] a) C. T. Kresge, M. E. Leonowicz, W. J. Roth, J. C. Vartuli, J. S. Beck, *Nature* **1992**, *359*, 710 – 712; b) J. S. Beck, J. C. Vartuli, W. J. Roth, M. E. Leonowicz, C. T. Kresge, K. D. Schmitt, C. T.-W. Chu, D. H. Olson, E. W. Shepard, S. B. McCullen, J. B. Higgins, J. L. Schlenker, *J. Am. Chem. Soc.* **1992**, *114*, 10834 – 10843.
[6] a) Q. Huo, D. I. Margolese, U. Ciesla, D. G. Demuth, P. Feng, T. E. Gier, P. Sieger, A. Firouzi, B. F. Chmelka, F. Schüth, G. D. Stucky, *Chem. Mater.* **1994**, *6*, 1176 – 1191; b) A. Firouzi, D. Kumar, L. M. Bull, T. Besier, P. Sieger, Q. Huo, S. A. Walker, J. A. Zasadzinski, C. Glinka, J. Nicol, D. Margolese, G. D. Stucky, B. F. Chmelka, *Science* **1995**, *267*, 1138 – 1143; c) U. Ciesla, D. Demuth, R. Leon, P. Petroff, G. Stucky, K. Unger, F. Schüth, *J. Chem. Soc. Chem. Commun.* **1994**, 1387 – 1388.
[7] P. T. Tanev, M. Chibwe, T. J. Pinnavaia, *Nature* **1994**, *368*, 321 – 323.
[8] C.-Y. Chen, S. L. Burkette, H.-X. Li, M. E. Davis, *Microporous Mater.* **1993**, *2*, 27 – 34.
[9] D. M. Antonelli, J. Y. Ying, *Curr. Opin. Colloid Interface Sci.* **1996**, *1*, 523 – 529.
[10] P. Behrens, *Angew. Chem.* **1996**, *108*, 561 – 564; *Angew. Chem. Int. Ed. Engl.* **1996**, *35*, 515 – 518.
[11] H. Yang, N. Coombs, G. A. Ozin, *Nature* **1997**, *386*, 692 – 695.
[12] D. Walsh, S. Mann, *Nature* **1995**, *377*, 320 – 323.
[13] E. Chomsky, G. A. Ozin, *Adv. Mater.* **2000**, *12*, 1071 – 1078.
[14] M. E. Davis, *Nature* **1993**, *364*, 391 – 393.
[15] J. Y. Ying, C. P. Mehnert, M. S. Wong, *Angew. Chem.* **1999**, *111*, 58 – 82; *Angew. Chem. Int. Ed.* **1999**, *38*, 56 – 77.
[16] M. Antonietti, B. Berton, C. Göltner, H.-P. Hentze, *Adv. Mater.* **1998**, *10*, 154 – 159.
[17] D. Zhao, J. Feng, Q. Huo, N. Melosh, G. H. Frederickson, B. F. Chmelka, G. D. Stucky, *Science* **1998**, *279*, 548 – 552.
[18] P. T. Tanev, T. J. Pinnavaia, *Science* **1996**, *271*, 1267 – 1269.
[19] A. Imhof, D. J. Pine, *Nature* **1997**, *389*, 948 – 951.
[20] B. T. Holland, C. F. Blanford, A. Stein, *Science* **1998**, *281*, 538 – 540.
[21] J. E. G. J. Wijnhoven, W. L. Vos, *Science* **1998**, *281*, 802 – 804.
[22] D. J. Norris, Yu. A. Vlasov, *Adv. Mater.* **2001**, *13*, 371 – 376.
[23] Q. Huo, D. I. Margolese, U. Ciesla, P. Feng, T. E. Gier, P. Sieger, R. Leon, P. M. Petroff, F. Schüth, G. Stucky, *Nature* **1994**, *368*, 317 – 320.
[24] D. M. Antonelli, J. Y. Ying, *Angew. Chem.* **1996**, *108*, 461 – 464; *Angew. Chem. Int. Ed. Engl.* **1996**, *35*, 426 – 430.
[25] D. M. Antonelli, A. Nakahira, J. Y. Ying, *Inorg. Chem.* **1996**, *35*, 3126 – 3136.
[26] T. Sun, J. Y. Ying, *Nature* **1997**, *389*, 704 – 706.
[27] D. M. Antonelli, *Microporous Mesoporous Mater.* **1999**, *33*, 209 – 214.
[28] D. M. Antonelli, J. Y. Ying, *Chem. Mater.* **1996**, *8*, 874 – 881.
[29] U. Ciesla, S. Schacht, G. D. Stucky, K. Unger, F. Schüth, *Angew. Chem.* **1996**, *108*, 596 – 600; *Angew. Chem. Int. Ed. Engl.* **1996**, *35*, 541 – 543.
[30] J. S. Reddy, A. Sayari, *Catal. Lett.* **1996**, *38*, 219 – 223.
[31] M. S. Wong, D. M. Antonelli, J. Y. Ying, *Nanostruct. Mater.* **1997**, *9*, 165 – 168.
[32] D. M. Antonelli, J. Y. Ying, *Angew. Chem.* **1995**, *107*, 2202 – 2206; *Angew. Chem. Int. Ed. Engl.* **1995**, *34*, 2014 – 2017.
[33] P. Liu, J. Liu, A. Sayari, *Chem. Commun.* **1997**, 577 – 578.

[34] D. M. Antonelli, *Adv. Mater.* **1999**, *11*, 488 – 492.
[35] D. M. Antonelli, *Microporous Mesoporous Mater.* **1999**, *30*, 315 – 319.
[36] Y. Wang, X. Tang, L. Lin, W. Huang, Y. R. Hacohen, A. Gedanken, *Adv. Mater.* **2000**, *12*, 1183 – 1186.
[37] Y. Takahara, J. N. Kondo, T. Takata, D. Lu, K. Domen, *Chem. Mater.* **2001**, *13*, 1200 – 1206.
[38] Z.-R. Tian, W. Tong, J.-Y. Wang, N.-G. Duan, V. V. Krishnan, S. L. Suib, *Science* **1997**, *276*, 926 – 929.
[39] M. Mamak, N. Coombs, G. Ozin, *Adv. Mater.* **2000**, *12*, 198 – 202.
[40] M. Wachhold, K. K. Rangan, S. J. L. Billinge, V. Petkov, J. Heising, M. G. Kanatzidis, *Adv. Mater.* **2000**, *12*, 85 – 91.
[41] M. J. MacLachlan, N. Coombs, G. A. Ozin, *Nature* **1999**, *397*, 681 – 684.
[42] M. Vettraino, M. Trudeau, D. Antonelli, *Adv. Mater.* **2000**, *12*, 337 – 341.
[43] M. Vettraino, M. Trudeau, D. Antonelli, *Inorg. Chem.* **2001**, *40*, 2088 – 2095.
[44] N. Q. Minh, *J. Am. Ceram. Soc.* **1993**, *76*, 563 – 588; B. C. H. Steele, *Nature* **1999**, *400*, 619 – 621.
[45] H. Verweij, *Adv. Mater.* **1998**, *10*, 1483 – 1486; A. Ziehfreund, U. Simon, W. F. Maier, *Adv. Mater.* **1996**, *8*, 424 – 427; F. P. F. van Berkel, F. H. van Heuveln, J. P. P. Huijsmans, *Solid State Ionics* **1994**, *72*, 240 – 247; B. C. H. Steele, *Solid State Ionics* **1997**, *94*, 239 – 248; H. Shiga, T. Okubo, M. Sadakata, *Ind. Eng. Chem. Res.* **1996**, *35*, 4479 – 4486.
[46] M. Mamak, N. Coombs, G. Ozin, *J. Am. Chem. Soc.* **2000**, *122*, 8932 – 8939.
[47] M. Mamak, N. Coombs, G. A. Ozin, *Adv. Funct. Mater.* **2001**, *11*, 59 – 63.
[48] Neeraj, C. N. R. Rao, *J. Mater. Chem.* **1998**, *8*, 1631 – 1634.
[49] H. Zheng, M. W. Colby, J. D. Mackenzie, *Mater. Res. Soc. Symp. Proc.* **1988**, *121*, 537 – 540; B. T. Holland, C. F. Blanford, T. Do, A. Stein, *Chem. Mater.* **1999**, *11*, 795 – 805.
[50] D. Zhao, D. Goldfarb, *Chem. Mater.* **1996**, *8*, 2571 – 2578.
[51] T. Abe, A. Taguchi, M. Iwamoto, *Chem. Mater.* **1995**, *7*, 1429 – 1430.
[52] D. M. Antonelli, M. Trudeau, *Angew. Chem.* **1999**, *111*, 1555 – 1559; *Angew. Chem. Int. Ed.* **1999**, *38*, 1471 – 1475.
[53] G. A. Ozin, *Acc. Chem. Res.* **1997**, *30*, 17 – 27.
[54] S. Oliver, A. Kuperman, N. Coombs, A. Lough, G. A. Ozin, *Nature* **1995**, *378*, 47 – 50.
[55] M. Terrones, H. Terrones, F. Banhart, J.-C. Charlier, P. M. Ajayan, *Science* **2000**, *288*, 1226 – 1229.
[56] R. J. Davis, J. Gainer, G. O'Neal, I.-W. Wu, *Water Environ. Res.* **1994**, *66*, 50 – 53.
[57] G. Al-sayyed, J. C. D'Oliveira, P. Pichat, *J. Photochem. Photobiol.* A **1991**, *58*, 99 – 114.
[58] F. Saladin, L. Forss, I. Kamber, *J. Chem. Soc. Chem. Commun.* **1995**, 533 – 534.
[59] M. Anpo, H. Yamashita, Y. Ichihashi, S. Ehara, *J. Electroanal. Chem.* **1995**, *396*, 21 – 26; H. Yamashita, N. Kamada, H. He, K. Tanaka, S. Ehara, M. Anpo, *Chem. Lett.* **1994**, 855 – 858.
[60] S. Yamagata, M. Nishijo, N. Murao, S. Ohta, I. Mizoguchi, *Zeolites* **1995**, *15*, 490 – 493.
[61] A. J. Bard, M. A. Fox, *Acc. Chem. Res.* **1995**, *28*, 141 – 145.
[62] K. Sayama, A. Tanaka, K. Domen, K. Maruya, T. Onishi, *J. Catal.* **1990**, *124*, 541 – 547.
[63] K. Tanaka, K. Harada, S. Murata, *Sol. Energy* **1986**, *36*, 159 – 161.
[64] V. F. Stone, Jr., R. J. Davis, *Chem. Mater.* **1998**, *10*, 1468 – 1474.
[65] Y. Takahara, J. N. Kondo, T. Takata, D. Lu, K. Domen, *Chem. Mater.* **2001**, *13*, 1194 – 1199.
[66] A. Kudo, H. Kato, S. Nakagawa, *J. Phys. Chem. B* **2000**, *104*, 571 – 575.
[67] T. Ishihara, H. Nishiguchi, K. Fukamachi, Y. Takita, *J. Phys. Chem. B* **1999**, *103*, 1 – 10.
[68] K. Sayama, H. Arakawa, *J. Photochem. Photobiol. A* **1994**, *77*, 243 – 247.
[69] P. A. Cox, *The Electronic Structure and Chemistry of Solids*, Oxford University Press, New York, **1987**.
[70] S. L. Brock, N. Duan, Z. R. Tian, O. Giraldo, H. Zhou, S. L. Suib, *Chem. Mater.* **1998**, *10*, 2619 – 2628.
[71] S. Murray, M. Trudeau, D. Antonelli, *Adv. Mater.* **2000**, *12*, 1339 – 1342.
[72] S. Murray, M. Trudeau, D. Antonelli, *Inorg. Chem.* **2000**, *39*, 5901 – 5908.
[73] D. O'Hare, *Chem. Soc. Rev.* **1992**, 121 – 126.
[74] H. J. Blythe, V. M. Fedosyuk, *J. Phys. Condens. Matter* **1995**, *7*, 3461 – 3469.
[75] G. Wirnsberger, K. Gatterer, H. P. Fritzer, W. Grogger, B. Pillep, P. Behrens, M. F. Hansen, C. B. Koch, *Chem. Mater.* **2001**, *13*, 1453 – 1466.
[76] G. Wirnsberger, K. Gatterer, H. P. Fritzer, W. Grogger, B. Pillep, P. Behrens, M. F. Hansen, C. B. Koch, *Chem. Mater.* **2001**, *13*, 1467 – 1472.
[77] S. Padovani, I. Chado, F. Scheurer, J. P. Bucher, *Phys. Rev. B* **1999**, *59*, 11 887 – 11 891.
[78] M. Vettraino, X. He, M. Trudeau, D. Antonelli, *J. Mater. Chem.* **2001**, *11*, 1755 – 1759.
[79] T. D. Shen, R. B. Schwarz, J. D. Thompson, *J. Appl. Phys.* **1999**, *85*, 4110 – 4119.
[80] X. He, M. Trudeau, D. Antonelli, *Adv. Mater.* **2000**, *12*, 1036 – 1039.
[81] X. He, M. Trudeau, D. Antonelli, *Inorg. Chem.* **2001**, *40*, 6463 – 6468.
[82] X. He, M. Trudeau, D. Antonelli, *Chem. Mater.* **2001**, *13*, 4808 – 4816.
[83] M. Vettraino, X. He, M. Trudeau, D. Antonelli, unpublished results.
[84] B. Ye, M. Trudeau, D. Antonelli, *Adv. Mater.* **2001**, *13*, 29 – 33.
[85] B. Ye, M. Trudeau, D. Antonelli, *Adv. Mater.* **2001**, *13*, 561 – 565.
[86] a) R. W. Lof, M. A. van Veenendaal, B. Koopmans, H. T. Jonkman, G. A. Sawatzky, *Phys. Rev. Lett.* **1992**, *68*, 3924 – 3927; b) M. J. Rosseinsky, *Chem. Mater.* **1998**, *10*, 2665 – 2685.
[87] B. Ye, M. Trudeau, D. Antonelli, *Chem. Mater.* **2001**, *13*, 2730 – 2741.
[88] W. Cheng, E. Baudrin, B. Dunn, J. I. Zink, *J. Mater. Chem.* **2001**, *11*, 92 – 97.
[89] P. Yang, D. Zhao, D. I. Margolese, B. F. Chmelka, G. D. Stucky, *Chem. Mater.* **1999**, *11*, 2813 – 2826.
[90] P. Yang, D. Zhao, D. I. Margolese, B. F. Chmelka, G. D. Stucky, *Nature* **1998**, *396*, 152 – 155.
[91] M. J. MacLachlan, N. Coombs, R. L. Bedard, S. White, L. K. Thompson, G. A. Ozin, *J. Am. Chem. Soc.* **1999**, *121*, 12 005 – 12 017.
[92] P. Osenar, P. V. Braun, S. I. Stupp, *Adv. Mater.* **1996**, *8*, 1022 – 1025.
[93] P. V. Braun, P. Osenar, S. I. Stupp, *Nature* **1996**, *380*, 325 – 328.
[94] S. I. Stupp, P. V. Braun, *Science* **1997**, *277*, 1242 – 1248.
[95] J. Li, H. Kessler, M. Soulard, L. Khouchaf, M. H. Tuiler, *Adv. Mater.* **1998**, *10*, 946 – 949.
[96] T. Jiang, G. A. Ozin, *J. Mater. Chem.* **1998**, *8*, 1099 – 1108; T. Jiang, G. A. Ozin, R. L. Bedard, *J. Mater. Chem.* **1998**, *8*, 1641 – 1648.
[97] M. Fröba, N. Oberender, *Chem. Commun.* **1997**, 1729 – 1730.
[98] Neeraj, C. N. R. Rao, *J. Mater. Chem.* **1998**, *8*, 279 – 280.
[99] M. Wachhold, K. K. Rangan, M. Lei, M. F. Thorpe, S. J. L. Billinge, V. Petkov, J. Heising, M. G. Kanatzidis, *J. Solid State Chem.* **2000**, *152*, 21 – 35.
[100] E. Prouzet, T. J. Pinnavaia, *Angew. Chem.* **1997**, *109*, 533 – 536; *Angew. Chem. Int. Ed. Engl.* **1997**, *36*, 516 – 518; S. A. Bagshaw, T. J. Pinnavaia, *Angew. Chem.* **1996**, *108*, 1180 – 1183; *Angew. Chem. Int. Ed. Engl.* **1996**, *35*, 1102 – 1105.
[101] K. K. Rangan, S. J. L. Billinge, V. Petkov, J. Heising, M. G. Kanatzidis, *Chem. Mater.* **1999**, *11*, 2629 – 2632.
[102] K. K. Rangan, P. N. Trikalitis, M. G. Kanatzidis, *J. Am. Chem. Soc.* **2000**, *122*, 10 230 – 10 231.
[103] P. N. Trikalitis, T. Bakas, V. Papaefthymiou, M. G. Kanatzidis, *Angew. Chem.* **2000**, *112*, 4732 – 4736; *Angew. Chem. Int. Ed.* **2000**, *39*, 4558 – 4562.
[104] H. Beinert, R. H. Holm, E. Münck, *Science* **1997**, *277*, 653 – 659.
[105] P. N. Trikalitis, K. K. Rangan, T. Bakas, M. G. Kanatzidis, *Nature* **2001**, *410*, 671 – 675.
[106] G. S. Attard, C. G. Göltner, J. M. Corker, S. Henke, R. H. Templer, *Angew. Chem.* **1997**, *109*, 1372 – 1374; *Angew. Chem. Int. Ed. Engl.* **1997**, *36*, 1315 – 1317.
[107] G. S. Attard, P. N. Bartlett, N. R. B. Coleman, J. M. Elliott, J. R. Owen, J. H. Wang, *Science* **1997**, *278*, 838 – 840.
[108] G. S. Attard, S. A. A. Leclerc, S. Maniguet, A. E. Russell, I. Nandhakumar, P. N. Bartlett, *Chem. Mater.* **2001**, *13*, 1444 – 1446.
[109] T. Bell, D. Antonelli, *Adv. Mater.* **1998**, *10*, 846 – 849.